

IRS Configuration Techniques for Ultra Wideband Signals and THz Communications

Alberto Tarable, Laura Dossi, Giuseppe Virone, *Senior Member, IEEE*, Alessandro Nordio, *Member, IEEE*

Abstract—Motivated by the challenges of future 6G communications where terahertz (THz) frequencies, intelligent reflective surfaces (IRSs) and ultra-wideband (UWB) signals coexist, we analyse and propose a set of efficient techniques for configuring the IRS when the signal bandwidth is a significant fraction of the central frequency (up to 50%). To the best of our knowledge this is the first time that IRS configuration techniques are analyzed for such huge bandwidths. In our work we take into account for the channel model, the power spectral density of the signal reflected by the IRS and the network geometry. We evaluate the proposed solutions in terms of achievable rate and compare it against an upper bound we derived. Our results hint rules for designing IRS-aided communication systems and allow to draw conclusions on the trade-off between performance and complexity required for configuring the IRS.

Index Terms—Intelligent Reflecting Surfaces, TeraHertz communications, 6G networks.

I. INTRODUCTION

THz communications is a promising technology able to fulfill the ambitious goals in terms of capacity of future 6G wireless networks, which are expected to reach Tb/s data rates, and handle UWB signals [2]. Future implementation of THz communications need to face harsh propagation environments typical of sub-millimeter wavelengths and characterized by high path losses and blockages. While path loss can be compensated for by using high-gain antenna arrays and through beamforming [3], the availability of LoS links is crucial for THz communications. In their absence, blockages can be circumvented e.g. by deploying IRSs, which are one of the key elements envisioned for building smart radio environments (SRE) [4], [5].

The interaction between UWB signals with large antenna arrays and IRSs poses, however, a number of new challenges. As an example, the signal propagation delay across large arrays has to be taken into account. Indeed, if the number of antenna elements in the array is large, the propagation delay becomes a significant fraction of the symbol period. Such a phenomenon, known as spatial-wideband effect [6] in the literature on array and radar signal processing, can entail

A. Tarable, L. Dossi, G. Virone, A. Nordio are with the National Research Council of Italy, Institute of Electronics, Information Engineering and Telecommunication (CNR-IEIIT), 10129 Torino, Italy (e-mail: <name>.<surname>@ieiit.cnr.it).

This work was partially supported by the European Union under the Italian National Recovery and Resilience Plan (NRRP) of NextGenerationEU, partnership on “Telecommunications of the Future” (PE00000001 - program “RESTART”), and by the Project: “SoBigData.it - Strengthening the Italian RI for Social Mining and Big Data Analytics” - Prot. IR0000013 - Avviso n. 3264 del 28/12/2021. Part of this material was accepted for publication at ICC 2023 (Workshop) and can be found in [1].

performance losses. Its frequency-domain manifestation is often referred to as *beam squint* [7], [8]. As a typical scenario, beams generated by antenna arrays or IRSs with frequency-independent adjustable phase shifters do not point to the same direction for different frequencies. As a consequence, only some frequencies can take advantage from high array gain toward the desired direction. This effect becomes more prominent as both the size of the antenna array and the signal bandwidth increase. Without taking countermeasures, an IRS-aided communication channel, as that depicted in Figure 1, is prone to beam-squint effects introduced by both the transmitter antenna array and the IRS. To solve these problems, several solutions to be applied at the transmitter have been proposed in order to make the generated beams nearly frequency-insensitive. Instead, in this work we propose to operate on the IRS by properly configuring its elements so as to compensate for the beam-squint effect, in the presence of UWB signals. In the following we provide an overview of the contributions of our work, followed by a review of the state of the art.

A. Contributions of this work

Motivated by the challenges of future 6G communications and by the recent advances in IRS technology [9], in this work

- we study a communication system where the signal bandwidth is a significant fraction (i.e., up to 50%) of the central frequency. To the best of our knowledge, this is the first time that such huge bandwidth is considered in IRS-aided communication;
- we consider a set of effective techniques for configuring the IRS phase-shifts; although some of these have already been proposed for narrowband communications, we have adapted them to signal bandwidths and power spectral densities that can be envisioned for 6G communications;
- we provide a set of numerical results assessing the performance of the above mentioned techniques, which hint design rules of IRS-aided communication systems and allow to draw conclusions on the trade-off between performance and complexity;
- we derive an upper bound to the achievable rate for a system, working in the THz frequencies, composed of a base station (BS), an IRS and an intended receiver (UE); such bound is used as a benchmark for assessing the performance of the considered IRS configuration techniques.; by numerical analysis, we prove the bound to be fairly tight, for a wide range of signal bandwidths;
- finally, we provide an analytical condition granting the optimality of an IRS configuration technique, as a func-

tion of the signal bandwidth, of the delay spread, and of the system geometry.

Summarizing, this work, which is an extension of [1], aims at understanding how a THz communication system should be designed to take advantage of IRSs in the presence of UWB signals. It provides fundamental performance limits for IRS-assisted systems in a realistic setting and proposes practical strategies that approach quite closely such performance limits.

B. Related works

Recent research in IRS-aided communications encompasses contributions in IRS modeling, wideband channel estimation and modeling, and mitigation of the beam-squint effect.

In many works the response of IRS elements is modeled as frequency-independent in both phase and amplitude although, in practice, it is far from being ideal [10], [11], [12]. The assumption of frequency independence of the IRS response is a good approximation only in the IRS operational bandwidth, which typically amounts to a small fraction of the operational central frequency. For this reason, so far, IRS did not seem suited to support UWB signals, which are characterized by relative bandwidths greater than 20%.

However, a very recent research in IRS design, has proposed an IRS model operating at 26.5 GHz [9] showing an operational bandwidth of about 30% of the carrier frequency, thus enabling IRS-aided UWB communications. Imagining further technology breakthrough, we expect that such figures could be further raised in the future and that very soon IRS-aided UWB communications will be available at much higher frequencies, e.g., in the sub-THz range.

The problem of optimally configuring the IRS in the presence of wideband signals has been considered in a few very recent papers. The authors in [13] consider a multicarrier wideband signal and propose to configure the IRS so as to maximize the achievable rate, for orthogonal frequency-division multiplexing signals, central frequency 28 GHz and relative bandwidth of about 7%, much smaller than that considered in this work. Similarly to what we do, they also propose a technique based on singular-value decomposition of a channel matrix. However, they apply such technique to the IRS-UE channel only, and neglect the influence of the BS-IRS channel and of the signal power spectral density.

Authors in [14] introduce a generalized channel model suitable for large IRSs operating in near field at THz frequencies, while [15], [16] propose to exploit the beam-squint effect, rather than eliminating it, to generate multiple beams simultaneously focused on multiple targets. Finally, [17] accounts for the beam-squint effect while addressing the problem of estimating the wideband channel in far field.

Beam-squint mitigation at the antenna arrays is considered in many works and solved e.g. through delay-phase precoding techniques [7] or true-time delayers (TTDs), in order to achieve ultra-wideband beamforming. The work in [18] discusses the implementation of TTDs and their applications for signals having instantaneous ultra-wide bandwidths, while in [8] approaches based on virtual sub-arrays and TTD lines are considered for eliminating beam squint. Such

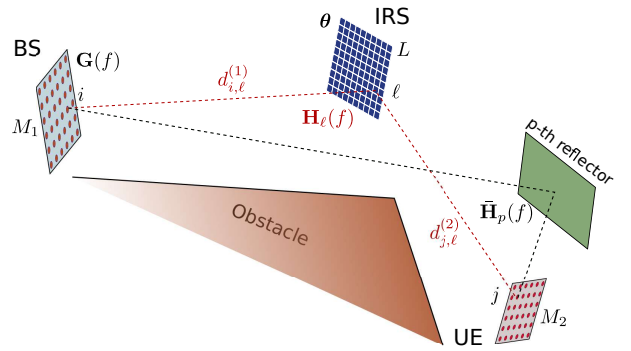


Fig. 1. Representation of a communication network where a BS and a UE communicate by exploiting an IRS. The LoS link between BS and UE is unavailable due to an obstacle. Channel multipath components are due to the presence of a small number of reflectors.

architecture can achieve performance very close to fully digital transceivers, although requiring high hardware cost and large power consumption. Unfortunately, these are not viable methods for eliminating beam squint at the IRSs, since they are made of passive elements, whose phase shifts cannot be controlled in the frequency domain. The recent proposal in [19] consists in a new implementation of the IRS, called delay-adjustable metasurface (DAM), where the elements rely on varactor diodes and are able to impose a controllable extra delay onto the reflected signals. DAMs are, however, subject to power losses and in a very early concept stage, as opposed to standard IRSs, whose prototypes are already available, as reported for example in [20].

The remainder of the paper is organized as follows. Section II describes the system model and formulates the optimization problem. Section III derives an upper bound to the achievable rate, Section IV proposes several algorithms aiming at maximizing the received power, whose performance are then assessed and compared in Section V. Conclusions are drawn in Section VI.

C. Mathematical notation

Boldface uppercase and lowercase letters denote matrices and vectors, respectively, uppercase calligraphic letters denote sets. \mathbf{I}_k is the $k \times k$ identity matrix. The (i, j) -th element of matrix \mathbf{A} is denoted by $[\mathbf{A}]_{i,j}$, \mathbf{A}^H is its conjugate transpose and $\text{Tr}\{\mathbf{A}\}$ its trace. We denote by $\rho(\mathbf{A})$ the rank of matrix \mathbf{A} . The symbol \odot denotes the Hadamard (i.e., elementwise) product. Finally, $\mu(\mathcal{A})$ denotes the measure of the set \mathcal{A} .

II. SYSTEM MODEL AND PROBLEM FORMULATION

We consider a wireless system operating in the THz band where a base station (BS), equipped with an array of M_1 antennas, transmits a data stream to a user (UE), equipped with M_2 antennas, as depicted in Fig. 1. The transmitted signal has bandwidth B_w and is characterized by the $M_1 \times M_1$ power spectral density matrix $\mathbf{G}(f)$, which we assume to be positive semidefinite and whose support, in the frequency space, is contained in set \mathcal{B} . The BS transmit power is denoted by

$$P^{\text{tx}} = \int_{\mathcal{B}} \text{Tr}\{\mathbf{G}(f)\} df. \quad (1)$$

At sub-THz and THz frequencies scattering and diffraction effects provide a marginal contribution to propagation. Indeed, most of the received energy is due to the LoS component and, possibly, to some non-LoS (NLoS) reflected rays [21]. Moreover, at THz frequencies many other effects come into play, such as molecular absorption [22], blockage, and large-scale fading effects (shadowing). In our model, we suppose that the UE is not in LoS with the BS due to blockage, while some rays leaving the BS may reach the UE after being reflected on large surfaces (e.g., building walls). In order to cope with the lack of LoS connectivity, the system exploits an IRS, composed of L electronically configurable reflective elements, as shown in Fig. 1.

A. IRS model

Practical IRSs are designed to work in a specific frequency band \mathcal{B} , around a central frequency f_c . Such operational band can be defined as the range of frequencies around f_c in which the transfer function of the ℓ -th IRS element, $\ell = 1, \dots, L$, satisfies

$$\zeta_\ell(f) \simeq \tilde{\zeta}(f)e^{j\theta_\ell}, \quad \forall f \in \mathcal{B} \quad (2)$$

where θ_ℓ is a supposedly controllable phase shift and $\tilde{\zeta}(f)$ is a known non-controllable complex frequency response, independent of θ_ℓ , with $|\tilde{\zeta}(f)|$ constant for $f \in \mathcal{B}$. In practice, the deviation of the true frequency response from (2), in both magnitude and phase, should have a limited effect on performance. Many works in the literature (see e.g. [10] and references therein) assume that, in the operational band, IRS elements are ideal phase shifters, i.e., with $\tilde{\zeta}(f) = 1$.

At present, most IRS implementations work in the sub-6 GHz band, whereas few are reported to operate in the mm-wave bands. For these implementations, the operational bandwidth greatly varies and usually amounts to a small fraction of f_c , typically less than 10%. However, an IRS design operating at $f_c = 26.5$ GHz and allowing an operational bandwidth of up to 30% was recently proposed [9]. This pioneering result enables IRS-assisted UWB communications in the mm-wave bands, making it a good candidate for 5G applications. Imagining further breakthroughs that, similarly to [9], could extend to THz frequencies the operational band of IRSs, maybe with on-chip technology, this paper assumes that the in-band frequency response of IRS elements satisfies (2). Even more generally, we will not need to pose any constraint on $|\tilde{\zeta}(f)|$, which can then be an arbitrarily-varying frequency function. Instead, it is important to stress that $\tilde{\zeta}(f)$ in (2) is independent of θ_ℓ in our model.

B. Overall system model

The channel transfer function of the BS–UE link is represented by the $M_1 \times M_2$ matrix $\mathbf{H}(f, \boldsymbol{\theta})$ given by

$$\mathbf{H}(f, \boldsymbol{\theta}) = \sum_{\ell=1}^L e^{j\theta_\ell} \mathbf{H}_\ell(f) + \bar{\mathbf{H}}(f) \quad (3)$$

where $\boldsymbol{\theta} = [\theta_1, \dots, \theta_L]^T$, $\mathbf{H}_\ell(f)$ is the channel transfer function for the path through the ℓ -th IRS element, which accounts for both IRS frequency response and signal propagation. The

matrix $\bar{\mathbf{H}}(f)$ takes into account the contribution of multipath, i.e. in this case, of rays reflected by large obstacles. Note that in (3) we stress the dependence of the channel matrix on the IRS configuration, $\boldsymbol{\theta}$, by explicitly indicating it as an argument. In details, $[\mathbf{H}_\ell(f)]_{i,j}$ is the scalar transfer function corresponding to the path connecting the i -th BS antenna to the j -th UE antenna through the ℓ -th IRS element, whose length is $d_{i,j,\ell}$ (see Figure 1), and can be modeled as

$$[\mathbf{H}_\ell(f)]_{i,j} = \alpha_{i,\ell}^{(1)} \alpha_{j,\ell}^{(2)} \tilde{\zeta}(f) e^{-j2\pi f \tau_{i,j,\ell} - \kappa(f) d_{i,j,\ell}} \frac{\sqrt{A_{i,\ell}^{(1)} A_{j,\ell}^{(2)}}}{4\pi d_{i,\ell}^{(1)} d_{j,\ell}^{(2)}} \quad (4)$$

where $\tau_{i,j,\ell} = \frac{d_{i,j,\ell}}{c}$ is the total travel time of the path. In particular, $d_{i,j,\ell} = d_{i,\ell}^{(1)} + d_{j,\ell}^{(2)}$ where $d_{i,\ell}^{(1)}$ ($d_{j,\ell}^{(2)}$) is the distance between transmit antenna i (receive antenna j) and IRS element ℓ . The superscripts (1) and (2) refer to the BS–IRS and IRS–UE hops, respectively. With the same notation $\alpha_{i,\ell}^{(1)}$ and $\alpha_{j,\ell}^{(2)}$ take into account the antenna gains at the BS and UE, respectively, and possible shadowing effects, while $A_{i,\ell}^{(1)} = A \cos(\phi_{i,\ell}^{(1)})$ and $A_{j,\ell}^{(2)} = A \cos(\phi_{j,\ell}^{(2)})$ are the effective areas of the IRS element ℓ as observed, respectively, from the i -th BS antenna and the j -th UE antenna [21], where A is the physical area of the IRS meta-atom and $\phi_{i,\ell}^{(1)}$ ($\phi_{j,\ell}^{(2)}$) is the angle of arrival from the i -th BS antenna (angle of departure towards the j -th UE antenna), measured counterclockwise w.r.t. the normal to the ℓ -th IRS meta-atom. Finally, $\kappa(f)$ is the molecular-absorption coefficient [23]. The multipath matrix $\bar{\mathbf{H}}(f)$ can be written as

$$\bar{\mathbf{H}}(f) = \sum_{p=1}^P \bar{\mathbf{H}}_p(f) \quad (5)$$

where P is the number of rays and $\bar{\mathbf{H}}_p(f)$ is the channel matrix corresponding to the p -th reflected ray. According to the image theorem we have

$$[\bar{\mathbf{H}}_p(f)]_{i,j} = \rho_p \alpha_{p,i,j} \frac{c}{4\pi f d_{p,i,j}} e^{-j2\pi f \tau_{p,i,j} - \kappa(f) d_{p,i,j}}$$

where ρ_p is the reflection coefficient of the p -th reflector, $d_{p,i,j}$ is the length of the path connecting the i -th BS antenna to the j -th UE antenna through the p -th reflector, and $\tau_{p,i,j} = \frac{d_{p,i,j}}{c}$ is the corresponding travel time. Finally $\alpha_{p,i,j}$ accounts for possible shadowing.

Remark 1: Note that the model in (2), (3) and (4) is very general and can apply to a 3D geometric environment with IRS and antenna arrays of any shape. Moreover, many results in the following, such as those of Section III, hold for any channel model satisfying (3), regardless of the particular expression of $\mathbf{H}_\ell(f)$ and $\bar{\mathbf{H}}(f)$.

C. Rate optimization problem

Given the power spectral density matrix of the input, $\mathbf{G}(f)$, the achievable rate is

$$R(\boldsymbol{\theta}) = \int_{\mathcal{B}} \log \left| \mathbf{I} + \frac{\mathbf{H}(f, \boldsymbol{\theta}) \mathbf{G}(f) \mathbf{H}^H(f, \boldsymbol{\theta})}{N_0} \right| df, \quad (6)$$

where $N_0/2$ is the per-dimension power spectral density of the circularly-symmetric additive white Gaussian noise at the

receiver. Our goal is to optimize the IRS phase shifts, $\boldsymbol{\theta}$, so as to maximize the rate $R(\boldsymbol{\theta})$. In other words, we would like to solve:

$$\max_{\boldsymbol{\theta}} R(\boldsymbol{\theta}). \quad (7)$$

This maximization is difficult to tackle; indeed, an explicit closed-form expression for the maximizer does not exist, so that one must resort to heuristic approaches in order to find good, albeit suboptimal, solutions. To that end, we start by deriving an upper bound to (6), hinting a solution for (7), which will be shown to be relatively tight in Section V. Such bound will be used as a benchmark to assess the performance of suboptimal solutions to (7).

III. UPPER BOUND TO THE END-TO-END COMMUNICATION RATE

In order to derive the upper bound to (6), we first give a couple of definitions. Let

$$P^{\text{rx}}(\boldsymbol{\theta}) = \int_{\mathcal{B}} \text{Tr}\{\mathbf{H}(f, \boldsymbol{\theta})\mathbf{G}(f)\mathbf{H}^{\text{H}}(f, \boldsymbol{\theta})\} df \quad (8)$$

be the received power and, let \mathbf{T} be the $L \times L$ matrix whose (ℓ, ℓ') entry is given by

$$[\mathbf{T}]_{\ell, \ell'} = \int_{\mathcal{B}} \text{Tr}\{\mathbf{H}_{\ell}(f)\mathbf{G}(f)\mathbf{H}_{\ell'}^{\text{H}}(f)\} df. \quad (9)$$

Then, we can state the following proposition:

Proposition 1: For $M_1 \geq M_2$ and $L \geq M_2$, the maximum rate can be upper-bounded as

$$\max_{\boldsymbol{\theta}} R(\boldsymbol{\theta}) \leq \sum_{m=1}^{M_2} B_m \log \left(1 + \frac{\max_{\boldsymbol{\theta}} P^{\text{rx}}(\boldsymbol{\theta})}{N_0 \sum_{i=1}^{M_2} B_i} \right) \quad (10)$$

$$= \sum_{m=1}^{M_2} B_m \log \left(1 + \frac{\max_{\boldsymbol{\gamma}, |\gamma_{\ell}|=1, \forall \ell} \boldsymbol{\gamma}^{\text{H}} \mathbf{T} \boldsymbol{\gamma} + w + 2\Re\{\mathbf{q}^{\text{H}} \boldsymbol{\gamma}\}}{N_0 \sum_{i=1}^{M_2} B_i} \right) \quad (11)$$

$$\leq \sum_{m=1}^{M_2} B_m \log \left(1 + \frac{L\lambda_T^{\max} + w + 2\sum_{\ell=1}^L |q_{\ell}|}{N_0 \sum_{i=1}^{M_2} B_i} \right) \quad (12)$$

where N_0 is the noise power spectral density, $\boldsymbol{\gamma} = [\gamma_1, \dots, \gamma_L]^{\text{T}}$, $\gamma_{\ell} = e^{j\theta_{\ell}}$, for $\ell = 1, \dots, L$. The coefficients B_m are defined as

$$B_m = \int_{\mathcal{B}} \mathbb{1}\{r_Q(f) \geq m\} df, \quad m = 1, \dots, M_2, \quad (13)$$

being $r_Q(f)$ any upper bound to the rank of the matrix $\mathbf{H}(f, \boldsymbol{\theta})\mathbf{G}(f)\mathbf{H}^{\text{H}}(f, \boldsymbol{\theta})$ for all $\boldsymbol{\theta}$. Moreover λ_T^{\max} is the maximum eigenvalue of \mathbf{T} , the scalar w is given by $w = \int_{\mathcal{B}} \text{Tr}\{\mathbf{H}(f)\mathbf{G}(f)\mathbf{H}^{\text{H}}(f)\} df$ and \mathbf{q} is a length- L vector with entries

$$q_{\ell}^* = \int_{\mathcal{B}} \text{Tr}\{\mathbf{H}_{\ell}(f)\mathbf{G}(f)\mathbf{H}^{\text{H}}(f)\} df, \quad \ell = 1, \dots, L. \quad (14)$$

In the special case where $\mathbf{G}(f)$ is rank-1 on its support, the bound (11) reduces to

$$\max_{\boldsymbol{\theta}} R(\boldsymbol{\theta}) \leq B_1 \log \left(1 + \frac{\max_{\boldsymbol{\theta}} P^{\text{rx}}(\boldsymbol{\theta})}{N_0 B_1} \right). \quad (15)$$

The above proposition holds for a general channel satisfying (3). In particular, if (4) is also satisfied, we can give an explicit expression for $r_Q(f)$, as per the following proposition.

Proposition 2: For a channel model satisfying (3)-(4), the upper bound $r_Q(f)$ can be written as

$$r_Q(f) = \min \{M_2, \rho(\mathbf{G}(f)), \min\{L, \rho(\mathbf{V}(f)), \rho_{wh}(f)\}\}. \quad (16)$$

where $\rho_{wh}(f) \triangleq \rho(\mathbf{W}(f)) + \rho(\bar{\mathbf{H}}(f))$, the matrix $\mathbf{H}_{\ell}(f)$ can be decomposed as $\mathbf{H}_{\ell}(f) = \mathbf{v}_{\ell}(f)\mathbf{w}_{\ell}^{\text{T}}(f)$ and the matrices $\mathbf{V}(f)$ and $\mathbf{W}(f)$ are given by $\mathbf{V}(f) = [\mathbf{v}_1(f), \dots, \mathbf{v}_L(f)]$ and $\mathbf{W}(f) = [\mathbf{w}_1(f), \dots, \mathbf{w}_L(f)]$, respectively. Note that, in practice, $L \gg M_2$, so the term L can be removed from the above expression.

The proofs of both propositions are provided in A.

Remark 2: Note that in the low-SNR regime, i.e., with received SNR $\eta = \frac{P^{\text{rx}}(\boldsymbol{\theta})}{B_1 N_0} \ll 1$, the rate $R(\boldsymbol{\theta})$ in (6) can be approximated to the first order as $R(\boldsymbol{\theta}) = B_1 \log(1 + \eta) + O(\eta^2)$, and the maximization over $\boldsymbol{\theta}$ leads to (15).

IV. SUB-OPTIMAL IRS CONFIGURATION TECHNIQUES

As already said, an explicit expression for the maximizer of (7) is difficult to obtain. However, we observe that the bound in (10) increases as the received power, $P^{\text{rx}}(\boldsymbol{\theta})$, increases. We then propose to solve

$$\max_{\boldsymbol{\theta}} P^{\text{rx}}(\boldsymbol{\theta}) = \max_{\boldsymbol{\gamma}, |\gamma_{\ell}|=1, \forall \ell} (\boldsymbol{\gamma}^{\text{H}} \mathbf{T} \boldsymbol{\gamma} + w + 2\Re\{\mathbf{q}^{\text{H}} \boldsymbol{\gamma}\}), \quad (17)$$

i.e., to maximize $P^{\text{rx}}(\boldsymbol{\theta})$, which corresponds to maximizing the upper bound to the rate, instead of the actual rate. Now, (17) is an example of Unimodular-Constraint Quadratic Problem (UCQP), which is known to be NP-hard. Note that a similar problem has been faced in [24] in the context of simultaneous IRS-aided communication and power transfer, and solved using a successive convex approximation technique. To solve (17) we propose two strategies:

- employing a numerical algorithms designed for solving UCQP problems, as described in Section IV-A;
- applying a heuristic solution based on the eigenvalue decomposition of matrix \mathbf{T} , as described in Section IV-B, which is proved to be high-performance.

Additionally, in Section IV-C, we propose a set of “narrowband solutions” to (7). Some of them show interesting performance under some conditions on the system parameters and geometry, as described in detail in Section V.

A. Numerical algorithms solving UCQP problems

There are several numerical algorithms able to provide close-to-optimal solutions to UCQP problems, such as MERIT [25] and SCF [26]. Among them, we consider SCF, which takes as input the $L \times L$ matrix \mathbf{T} and applies an iterative procedure: at each iteration, it computes the inverse of a $2L \times 2L$ real matrix. Although it can provide near-optimum solution to (17), its complexity rapidly increases with L and also increases with the number of iterations required to reach convergence. The algorithm reported in [26] has been adapted to the problem at hand. Its performance is reported in Section V and compared against other techniques.

B. A heuristic solution based on eigenvalue decomposition

An heuristic solution for the maximizer of (17) can be derived in the absence of channel multipath components ($\bar{\mathbf{H}}(f) = \mathbf{0}$). In order to obtain it, we proceed as follows:

- we first relax the UCQP problem to

$$\max_{\gamma, \gamma^H \gamma = L} \gamma^H \mathbf{T} \gamma \quad (18)$$

and compute its maximizer $\tilde{\gamma} = \sqrt{L} \mathbf{u}^{\max}$ where \mathbf{u}^{\max} is the unit-norm eigenvector of \mathbf{T} corresponding to its maximum eigenvalue. Clearly $\tilde{\gamma}$ does not, in general, satisfy the unimodular constraint $|\gamma_\ell| = 1, \forall \ell$;

- we then extract the phases of each entry of $\tilde{\gamma}$, obtaining

$$\gamma_\ell^* = e^{j \arg(\tilde{\gamma}_\ell)}, \quad \ell = 1, \dots, L. \quad (19)$$

and we use $\gamma^* = [\gamma_1^*, \dots, \gamma_L^*]^T$ as an approximate solution for the original problem (17).

A similar procedure was also suggested in [13] for a NLoS scenario where, however, it was applied to the IRS–UE channel only. Instead, we apply it to matrix \mathbf{T} which includes the effect of both the TX–RX channel matrix and the signal power spectral density. This approach requires the knowledge of \mathbf{T} and its complexity is dominated by the extraction of the largest eigenvalue of \mathbf{T} .

C. A family of solutions inspired by narrowband signals

In this subsection, we consider a set of suboptimal solutions to the problem (17), tailored to the case where the transmitted signal is narrowband at frequency f_0 and the communication channel does not exhibit multipath components (i.e., $\bar{\mathbf{H}}(f) = \mathbf{0}$). Such solutions take, in general, the form

$$\gamma_\ell^{\text{NB}}(f_0) = e^{j2\pi f_0 \tau_\ell}, \quad \ell = 1, \dots, L. \quad (20)$$

They satisfy the unimodular constraint, and will be called *narrowband (NB) at frequency f_0 with coefficients τ_ℓ* . They are interesting in that they show in some cases good performance, even in the presence of wideband signals. Narrowband solutions of the family (20) have already been proposed in [13], [27], however they have been investigated only for small signal bandwidths, compared to the central frequency f_c .

In Section V, we will compare the rate they achieve against the upper bound in (12), for a wide variety of system parameters and geometries.

The narrowband solutions we propose are derived under the hypothesis of small BS and UE array size, and consider also the case of discrete signal spectrum, as detailed in the following Sections IV-C1 and IV-C2, respectively. In Section IV-C3 we also describe the optimal NB solution maximizing (17).

1) *Small BS and UE array size*: We here assume that the BS and UE antenna arrays are small w.r.t. the BS–IRS and IRS–UE distances, i.e., they can be seen under a small angle when observed from the IRS. Then, we can decouple the indices i, j, ℓ in the expression for $\tau_{i,j,\ell}$ in (4) and write it as a sum of three terms as

$$\tau_{i,j,\ell} \approx c_{\text{BS},i} + c_{\text{UE},j} + \tau_\ell$$

where $c_{\text{BS},i}$ and $c_{\text{UE},j}$ are functions of the geometrical arrangement of the array elements at the BS and at the UE, respectively, as well as of the array orientation in space w.r.t. the IRS. The term τ_ℓ represents the signal travel time through IRS element ℓ , measured from the center of the BS array to the center of the UE array. Under the same assumption, and referring to (4), we can approximate the distances $d_{i,\ell}^{(1)}$ and $d_{j,\ell}^{(2)}$ as $d_{i,\ell}^{(1)} \approx d_\ell^{(1)}$ and $d_{j,\ell}^{(2)} \approx d_\ell^{(2)}$ so that $d_{i,j,\ell} \approx d_\ell = d_\ell^{(1)} + d_\ell^{(2)}$. Moreover, also the antenna gains and the shadowing coefficients do not depend on i and j , i.e., $\alpha_{i,\ell}^{(1)} = \alpha_\ell^{(1)}$, $\alpha_{j,\ell}^{(2)} = \alpha_\ell^{(2)}$ and the dependence on i and j can also be dropped from $A_{i,\ell}^{(1)} = A_\ell^{(1)}$ and $A_{j,\ell}^{(2)} = A_\ell^{(2)}$, since the IRS elements have the same area and see all BS (UE) antenna elements under the same angle. Finally, if the attenuation due to molecular absorption is negligible for every $f \in \mathcal{B}$ (as for indoor application and short-range communications), the term $e^{\kappa(f)d_{i,j,\ell}}$ in (4) can be neglected. By plugging the above approximations in (4), the channel matrix $\mathbf{H}_\ell(f)$ can be simplified as

$$\mathbf{H}_\ell(f) = K_\ell \mathbf{A}(f) e^{-j2\pi f \tau_\ell} \quad (21)$$

where we defined $[\mathbf{A}(f)]_{i,j} = \tilde{\zeta}(f) e^{-j2\pi f (c_{\text{BS},j} + c_{\text{UE},i})}$ and $K_\ell = \frac{\alpha_\ell^{(1)} \alpha_\ell^{(2)} \sqrt{A_\ell^{(1)} A_\ell^{(2)}}}{4\pi d_\ell^{(1)} d_\ell^{(2)}}$. For this scenario, we have the following propositions:

Proposition 3: If the channel matrix $\mathbf{H}_\ell(f)$ takes the form in (21) and the signal is monochromatic at frequency f_0 , the solution to the problem (18) is (20).

The proof is provided in B. Such result can be generalized to wideband signals as follows.

Proposition 4: Consider a wideband signal and a channel for which (21) holds. Let $T_{\text{DS}} = \max_{\ell, \ell'=1, \dots, L} (\tau_\ell - \tau_{\ell'})$ be the delay spread experienced by the signal, when reflected by the IRS. If the power spectral density of the received signal has an even symmetry around frequency f_0 and its bandwidth satisfies

$$B_w \leq \frac{1}{2T_{\text{DS}}} \quad (22)$$

then the solution to (18) will be given by (20).

The proof is provided in C.

In a 2D scenario where the antenna arrays and the IRS have a linear shape and the IRS size is small compared to the BS–IRS and IRS–UE distances, a special case of (21) can be considered. Indeed, under such hypothesis the dependence on ℓ of K_ℓ can be dropped and the angles $\phi_{i,\ell}^{(1)}$ and $\phi_{j,\ell}^{(2)}$ (the directions of the i -th BS antenna and of the j -th UE antenna as observed from the ℓ -th IRS element) are independent of the array indices, i.e. $\phi_{i,\ell}^{(1)} = \phi_{\text{BS}}$ and $\phi_{j,\ell}^{(2)} = \phi_{\text{UE}}$. Also, $\tau_\ell \approx C + \ell\tau$ where C is a constant, $\tau = \frac{\Delta(\sin \phi_{\text{BS}} - \sin \phi_{\text{UE}})}{c}$, Δ being the IRS element spacing. Then, $T_{\text{DS}} = \max_{\ell, \ell'=1, \dots, L} |\ell\tau - \ell'\tau| = (L-1)|\tau|$ and condition (22) becomes

$$B_w \leq \frac{c}{2(L-1)\Delta |\sin \phi_{\text{BS}} - \sin \phi_{\text{UE}}|}. \quad (23)$$

For example, for $\Delta = c/(2f_0)$ (i.e., the IRS element spacing is half the wavelength $\lambda_0 = c/f_0$) and in the most unfavorable (albeit unrealistic) geometric deployment of the network nodes

(i.e., $\phi_{\text{BS}} = \phi_{\text{UE}} = \pi/2$), we have

$$\frac{B_w}{f_0} \leq \frac{1}{2(L-1)}. \quad (24)$$

Note that the above expression is important since it directly relates the normalized bandwidth B_w/f_0 to the inverse of the IRS size, L . We also observe that the solution $\gamma^{\text{NB}}(f_0)$ is easy to compute since it only requires some information about the geometry of the system, i.e., the delays τ_ℓ , and the value of the central frequency of the signal spectrum.

2) *Small BS and UE array size and discrete signal spectrum*: If the transmitted signal has a spectrum organized in S subcarriers located at frequencies f_s , $s = 1, \dots, S$, the power spectral density matrix $\mathbf{G}(f)$ can be written as

$$\mathbf{G}(f) = \sum_{s=1}^S \mathbf{G}_s \delta(f - f_s)$$

where f_s is the frequency associated to the s -th subcarrier. Under the hypothesis made in Section IV-C1 (i.e., small BS, UE and IRS sizes and a 2D scenario) the entries of matrix \mathbf{T} in (18) read as follows:

$$[\mathbf{T}]_{\ell, \ell'} = K^2 \sum_{s=1}^S M_s e^{j2\pi(\ell' - \ell)\tau f_s} \quad (25)$$

where $M_s = \text{Tr}\{\mathbf{A}(f_s)\mathbf{G}_s\mathbf{A}^H(f_s)\}$ is proportional to the received signal power for subcarrier s . Hence $\mathbf{T} = \sum_{s=1}^S M_s \mathbf{z}_s \mathbf{z}_s^H$, $\mathbf{z}_s = [z_{s,1}, \dots, z_{s,L}]^T$, and $z_{s,\ell} = K e^{-j2\pi\ell\tau f_s}$. In the case of a large number of IRS elements, we state the following proposition:

Proposition 5: When $L \rightarrow \infty$, for a matrix \mathbf{T} given by (25), the solution of the UCQP in (18) is given by $\gamma^{\text{NB}}(f_{s^*})$ where s^* is the subcarrier index maximizing over s the term M_s defined after (25), i.e., $s^* = \arg \max_s M_s$.

The proof is provided in D. The evaluation of $\gamma^{\text{NB}}(f_{s^*})$ requires to compute the terms M_s , which in turn requires the knowledge of the matrix $\mathbf{A}(f)$, defined after (21), and of the power spectral density \mathbf{G}_s .

3) *Optimal narrowband solution*: Finally, we consider the narrowband solution, $\gamma^{\text{NB}}(f^*)$, obtained by searching in the band \mathcal{B} for the frequency f^* maximizing the received power, i.e.,

$$f^* = \arg \max_{f \in \mathcal{B}} (\gamma^{\text{NB}}(f))^H \mathbf{T} \gamma^{\text{NB}}(f). \quad (26)$$

The optimal frequency f^* can be obtained by plain numerical search. With respect to previous NB solutions, it requires an exhaustive search on the frequency space and the knowledge of the matrix \mathbf{T} defined in (9).

V. PERFORMANCE ASSESSMENT

We now assess through simulation the performance of the IRS configuration options outlined in Section IV. We specifically measure and discuss the influence that the system parameters (such as the IRS size, the presence of multipath components, and the signal bandwidth B_w) have on the achievable rate. The next two subsections will be devoted to the description of the simulation setup, i.e., the network

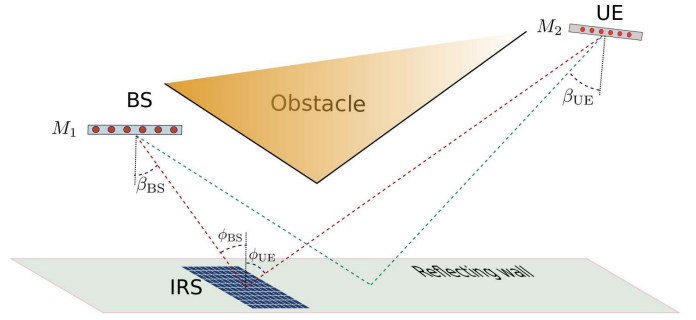


Fig. 2. Geometry of the simulated wireless communication network. The IRS is attached to a wall which also acts as a reflector. The IRS has square shape and is composed of $L = L_s^2$ elements.

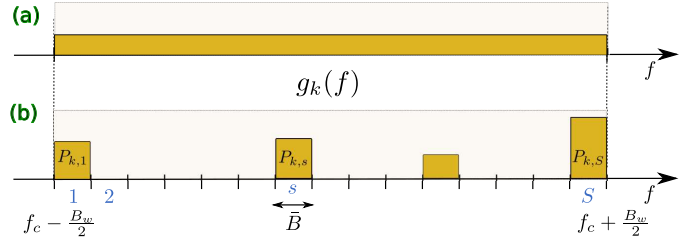


Fig. 3. Power spectral density profile of the signal transmitted by the k -th beam: (a) the entire available bandwidth is dedicated to a single user and (b) only some sub-bands are assigned to the UE.

geometric model, the channel characteristics and the properties of the transmitted signal.

A. Geometric model and channel characteristics

In the simulations we consider the 2D scenario depicted in Figure 1 and a wireless communication network operating in the THz band at central frequency $f_c = 300$ GHz. The BS is equipped with a uniform linear array (ULA) of M_1 antennas spaced by $\Delta = \lambda_c/2$ where $\lambda_c = c/f_c = 1$ mm is the wavelength corresponding to the central frequency and c is the speed of light. The UE has an ULA composed of $M_2 = 8$ elements, spaced by Δ . Furthermore, for the BS we assume 3GPP sectored antenna element [28] characterized by 8 dBi maximum directional gain, whereas for the UE we consider isotropic (i.e. 0dBi) antennas. The IRS, located on a wall which may also act as a reflector (see Figure 2), has a square shape and is composed of $L = L_s^2$ elements, with L_s elements per side, spaced by Δ . The area of an element is, thus, $A = \Delta^2$ (there are no gaps among elements). As for the frequency response of the IRS element, we employ the model in (2), assuming that the IRS operational bandwidth is greater than the signal bandwidth. Since at present no practical models exist for IRS operating at $f_c = 300$ GHz, we consider a transfer function similar to that depicted in [9, Figs. 3(a) and 4(a)], where $\tilde{\zeta}(f) \approx \rho(f) e^{j\alpha(f-f_c)}$, with $\rho(f) \approx -1$ dB its magnitude and $\alpha \approx -25^\circ/\text{GHz}$ a real constant.

The BS and UE are located at $d^{(1)} = 8$ m and $d^{(2)} = 15$ m, respectively, from the the IRS center. The attenuation due to atmospheric molecular absorption in the 230–370 GHz band ranges from 1 dB/km to tens of dB/km [29]. However, in such band and for the short distances involved in indoor

applications, the molecular absorption loss is not a major issue and can be neglected. As for the reflection properties of the wall, we adopt the complex reflection coefficient characterization of plasterboard panels [30] depicted in [21, Figure 2]. Finally, at the UE, the noise power spectral density is set to $N_0 = -174$ dBm/Hz.

B. Power spectral density of the transmitted signal and beamforming vector

We assume that the BS transmits a signal of bandwidth B_w whose support is $\mathcal{B} \subseteq [f_c - \frac{B_w}{2}, f_c + \frac{B_w}{2}]$. For every frequency $f \in \mathcal{B}$, the BS employs the antenna array to generate up to K beams so that the transmitted signal can be described by the power spectral density matrix

$$\mathbf{G}(f) = \sum_{k=1}^K g_k(f) \mathbf{v}_k(f) \mathbf{v}_k^H(f) \quad (27)$$

where $g_k(f)$ is the scalar power spectral density associated to the k -th beam, whose support is $\mathcal{B}_k \subseteq \mathcal{B}$ for $k = 1, \dots, K$ (see the examples depicted in Fig. 3). So, the rank of $\mathbf{G}(f)$ can be up to K , provided that the dimension of the vector space generated by the set of beamformers, $\mathbf{v}_k(f)$, is K . Then, according to (1), the total transmit power is given by $P^{\text{tx}} = \sum_{k=1}^K P_k^{\text{tx}}$, where $P_k^{\text{tx}} = \int_{\mathcal{B}_k} g_k(f) df$ is the transmit power associated to the k -th beam. So far, there are no standards regulating communications at such high frequencies, however the formula in (27) is general enough to encompass many scenarios that can be envisioned, as those described in [31]. For example, and referring to the k -th beam:

- the entire available bandwidth is dedicated to the UE as represented in Fig 3(a). This is the case of single-carrier UWB signaling, obtained e.g. by transmitting very narrow pulses. If the spectrum is flat, the scalar power spectral density $g_k(f)$ can be expressed as $g_k(f) = P_k^{\text{tx}}/B_w$;
- only portions of the available bandwidth are dedicated to the UE, as depicted in Fig 3(b), where the spectrum is divided in S sub-bands, each having the same bandwidth \bar{B} , i.e. $S\bar{B} = B_w$. One or more (not necessarily adjacent) sub-bands are allocated to the UE. In a scenario where multiple UEs compete for spectrum resources, this choice depends on the data rate required by the UE and on the allocation strategy of the sub-bands.

In the example of Figure 3(b), four sub-bands are assigned to the UE through the power spectral density $g_k(f)$. The area of the yellow rectangles represents the power associated to each sub-band. In this scenario the scalar power spectral density $g_k(f)$ can be written as

$$g_k(f) = \sum_{s=1}^S \frac{P_{k,s}^{\text{tx}}}{\bar{B}} \Pi_{\bar{B}}(f - f_s) \quad (28)$$

where $\Pi_{\bar{B}}(f) = 1$ for $|f| \leq \frac{\bar{B}}{2}$ and 0 elsewhere, and $f_s = f_c + \bar{B}(s - (S+1)/2)$, $s = 1, \dots, S$ is the central frequency of the s -th sub-band. Finally, $P_{k,s}^{\text{tx}}$ is the power associated by the transmitter to beam k in sub-band s . Note that $P_{k,s}^{\text{tx}} = 0$ if the sub-band s is not allocated to

the UE for beam k . The power of the k -th beam is given by $P_k^{\text{tx}} = \sum_{s=1}^S P_{k,s}^{\text{tx}}$.

Let \mathcal{S}_k be the set of sub-bands assigned to the UE for beam k , having cardinality $N_k = |\mathcal{S}_k|$. In the simulations we consider two possible power allocation scenarios:

- all allocated sub-bands have the same power, i.e. $P_{k,s}^{\text{tx}} = P_k^{\text{tx}}/N_k$ for $s \in \mathcal{S}_k$ and $P_{k,s}^{\text{tx}} = 0$ elsewhere; we will refer to this allocation as “equal power loading”;
- the powers $P_{k,s}^{\text{tx}}$, $s \in \mathcal{S}_k$ are obtained by extracting outcomes of independent uniformly distributed random variables normalized so that their sum is P_k^{tx} . We will refer to this allocation as “random power loading”.

The transmitter array can also generate beam squint. However, its effects can be mitigated, e.g., through frequency-dependent architectures, which adopt virtual arrays and TTD lines [8], so as to achieve performance very close to fully digital transceivers. Therefore, for the beamforming vector, we can consider the two following techniques at the BS:

- a single frequency-independent beamforming vector tuned on a specific frequency, say the central frequency f_c , whose m -th entry, $m = 0, \dots, M_1 - 1$, is given by

$$[\mathbf{v}_k(f)]_m = \frac{1}{\sqrt{M_1}} e^{j2\pi m(\Delta/c)f_c \sin(\beta_{\text{BS},k})} \quad (29)$$

for $f \in \mathcal{B}$, where $\beta_{\text{BS},k}$ is the direction of beam k at central frequency f_c , as observed from the center of the BS array. When many beams are generated, the angles $\beta_{\text{BS},k}$ should significantly differ, in order to grant spatial diversity and a rank $K > 1$. The beamformer in (29) is simple to implement since it is independent of f . However, when wideband signals are transmitted, it generates beam squint, which makes the beam direction frequency-dependent. In the following, we will refer to (29) as “Central beamforming” technique;

- a set of S beamforming vectors tuned on the central frequencies f_s of the sub-bands, $s=1, \dots, S$, whose m -th entry, $m=0, \dots, M_1-1$, is given by

$$[\mathbf{v}_k(f)]_m = \frac{1}{\sqrt{M_1}} e^{j2\pi m(\Delta/c)f_s \sin(\beta_{\text{BS},k})}, \quad (30)$$

for $f \in [f_s - \bar{B}/2, f_s + \bar{B}/2]$ and $s=1, \dots, S$. This beamforming technique will be referred to as “Adapted beamforming”. It can be implemented with, e.g., a fully digital transmit array, and can significantly reduce the beam squint effect generated by the BS array (provided that \bar{B} is sufficiently small), at the expense of a much higher transmitter complexity.

C. IRS configuration solutions and complexities

We assess the performance of the IRS configuration options described in the previous sections, in particular:

- the narrowband (NB) solution tailored to the central frequency f_c , $\gamma^{\text{NB}}(f_c)$, whose elements are as in (20) with $f_0 = f_c$ and $\tau_\ell = d_\ell/c$, according to the geometry depicted in Figure 2. This solution is the simplest one

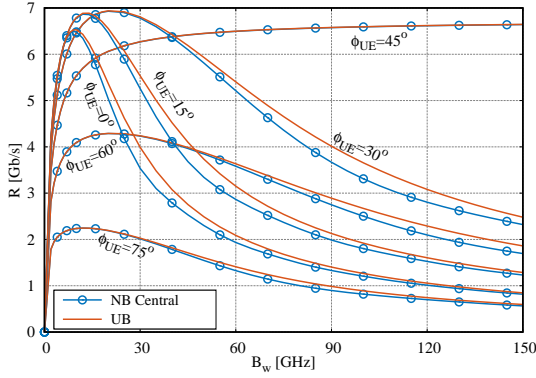


Fig. 4. Rate, R , versus B_w , as ϕ_{UE} varies, for $K = 1$, $M_1 = 16$, $P^{tx} = 22$ dBm, $L = 64 \times 64$ and $\phi_{BS} = 45^\circ$. The BS implements single carrier UWB communication with “Adapted beamforming”.

since it has the advantage of depending only on the system geometry, i.e., on the position of the BS and UE, while being independent of the signal spectrum. Such solution was also proposed in [13] and reported to provide good performance for bandwidths up to 7%. However, this is not the case for much larger bandwidths, as we will show in Section V-D. In the following it will be referred to as “NB Central”. The complexity of computing $\gamma^{NB}(f_c)$ is about $O(L)$;

- for spectra as in Fig. 3(b), the narrowband solution $\gamma^{NB}(f_{s^*})$ defined in Proposition 5; this solution requires to evaluate the received power for each sub-band, and the knowledge of the channel matrix. In the following it is referred to as “NB Max-power”. Its complexity is about $O(\max_k N_k L)$ where N_k is the number of allocated sub-bands for beam k ;
- the narrowband solution $\gamma^{NB}(f^*)$, described in Section IV-C3 and in the following labeled “NB Optimum”. We recall that such technique requires to search in the frequency space \mathcal{B} . To reduce complexity, in the simulations, we discretized the frequency space and tested only the central frequency of each sub-band of width \bar{B} . Therefore, the complexity of computing $\gamma^{NB}(f^*)$ is about $O(SL^2)$ where S is the number of sub-bands contained in the frequency range $[f_c - \frac{B_w}{2}, f_c + \frac{B_w}{2}]$, and $S = B_w/\bar{B}$;
- the outcome of the “SCF” algorithm proposed in [26], which numerically solves the UCQP problem (17). It works iteratively and requires the knowledge of the matrix \mathbf{T} and of the vector \mathbf{q} . Its complexity is $O(L^3 + FL^{2.373})$ where F is the number of iterations (sometimes large) required to reach convergence. In general, the convergence rate depends on the value of the threshold used to declare convergence and on the problem size, L . Also, the outcome of SCF depends on the starting point of the iterative procedure, i.e., an initial random guess of the vector γ . However, due to the non-convexity of UCQP, not all starting points lead to the same solution. Then, we decided to run the algorithm several times for each instance of the problem (17) and keep the best solution found;

- the solution provided by semidefinite relaxation (SDR) techniques described in [32] and also proposed in [33] to optimize IRS-aided communications in the presence of narrowband signals, independently of the transmitted signal spectrum;
- the vector γ^* obtained by extracting the phases of the eigenvector \mathbf{u}^{\max} corresponding to the maximum eigenvalue of the matrix \mathbf{T} , as specified in (19). This technique requires the knowledge of the matrix \mathbf{T} and will be referred to as “Max-eig phase”; its complexity is about $O(L^3)$;
- the upper bound in (12), which will be used as a benchmark and denoted by the label “UB”.

D. Numerical results for a rank-1 matrix $\mathbf{G}(f)$

We start by considering a matrix $\mathbf{G}(f)$ having rank-1 on its support ($K = 1$) and a single-carrier UWB signal while neglecting both shadowing and multipath. In this case, the power spectral density of the transmitted signal can be represented as in Fig 3(a). Figures 4 reports the achievable rate R (Gb/s), computed by using (6), plotted versus signal bandwidth, B_w , for $M_1 = 16$ transmit antennas, transmit power $P^{tx} = 22$ dBm, $\phi_{BS} = 45^\circ$, and $L_s = 64$ (hence $L = L_s^2 = 4096$ IRS elements). In Figure 4 the BS employs the “Adapted beamforming” technique so as to eliminate the beam-squint effect at the BS. The figure reports 6 sets of curves, characterized by the angles $\phi_{UE} \in \{0^\circ, 15^\circ, 30^\circ, 45^\circ, 60^\circ, 75^\circ\}$. Each set is composed of two curves: the rate achieved by using “NB central” technique, and the upper bound “UB”. First of all, we observe that “NB Central”, despite its simplicity, shows excellent performance, very close to the upper bound “UB”. We also note that for $\phi_{BS} = \phi_{UE} = 45^\circ$ both incident and reflected angles are the same and hence the IRS acts as an ordinary mirror if we impose a constant phase-shift, θ_ℓ , across the surface. In this particular situation the IRS does not generate any beam-squint effect and the rate increases with B_w according to the well-known law $B_w \log_2(1 + P^{rx}/(N_0 B_w))$. However, when the incident and reflected angles differ, the direction of the beam generated by the BS is frequency-dependent and, hence, part of the signal energy is spread in unwanted directions. This causes a rate loss, which increases as B_w increases. For any $\phi_{UE} \neq \phi_{BS}$, the rate curve shows a peak whose maximum is higher for $\phi_{UE} < 45^\circ$. This is due to the fact that the effective area of an IRS element, $A_{j,\ell}^{(2)}$ depends on $\cos(\phi_{j,\ell}^{(2)})$ and, hence, is maximized when the UE is approximately located in front of the IRS. In the scenario depicted in the figure, communication does not incur severe performance losses if the bandwidth is about 5% to 15% of the central frequency, although some tolerance is allowed depending on the system geometry. The “UB” curves tell us that, when the signal bandwidth, B_w , exceeds 30 GHz, penalties due to IRS beam squint severely reduce the achievable rate, no matter how the IRS is configured. Note that for each angle ϕ_{UE} , there is an optimal B_w that maximizes the rate. This means that, in order to avoid rate penalties, the signal bandwidth must be swiftly adapted to the system geometry especially in high mobility scenarios.

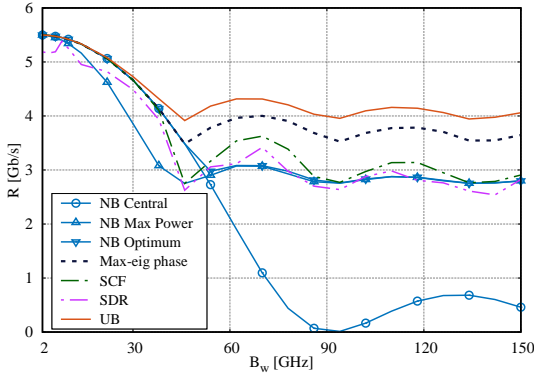


Fig. 5. Rate R versus B_w , for $K = 1$, $M_1 = 16$, $L = 64 \times 64$, $\phi_{BS} = 45^\circ$, $\phi_{UE} = 30^\circ$, $P_{1,s}^{tx} = 22$ dBm, “equal power loading” among sub-bands, and “Adapted beamforming” at the BS. The signal power spectral density is organized as in Figure 3(b) with $N_1 = 2$. The effects of multipath and shadowing are not taken into account.

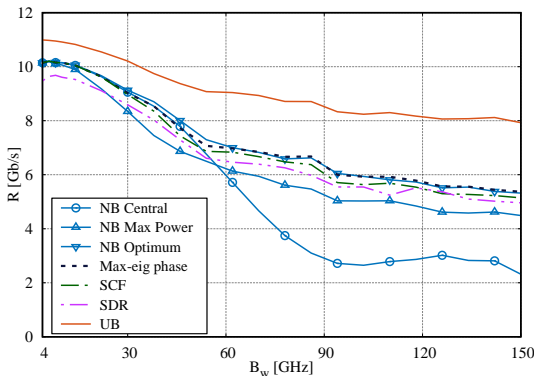


Fig. 6. Rate R versus B_w , for $K = 1$, $M_1 = 16$, $L = 64 \times 64$, $\phi_{BS} = 45^\circ$, $\phi_{UE} = 30^\circ$, $P_{1,s}^{tx} = 22$ dBm per sub-band, “random power loading” among sub-bands and “Adapted beamforming” at the BS. The signal power spectral density is organized as in Figure 3(b) with $N_1 = 4$. The effects of multipath and shadowing are neglected.

In Figure 5 we show the achievable rate plotted versus the available bandwidth in the case where the spectrum is organized in S sub-bands, each having bandwidth $\bar{B} = 1$ GHz, out of which $N_1 = 4$ have been allocated to the UE so that the support of the signal spectrum has measure 2 GHz. The sub-bands are organized as depicted in Figure 3(b): the innermost ones are randomly located in the available slots. The curves have been obtained by averaging over 100 realizations of such allocations. The transmitted power per allocated sub-band is set to $P_{1,s}^{tx} = 22$ dBm and equal power loading across sub-bands is employed. The BS and the UE are observed from the IRS under the angles $\phi_{BS} = 45^\circ$ and $\phi_{UE} = 30^\circ$ (see Fig. 2). Again, shadowing and channel multipath components are neglected. As can be observed, the “NB central” solution performs very close to the upper bound for $B_w \leq 30$ GHz, whereas it suffers significant performance losses for $B_w \geq 45$ GHz and even drops to zero for $B_w = 90$ GHz. This oscillating effect is due to the radiation pattern of the IRS. A rate close to zero occurs when the direction of the UE, as observed from the IRS, corresponds to a null between two adjacent side lobes. Interestingly, the other IRS configuration techniques do not seem to suffer from this effect although

some small oscillations can still be observed in the rate. The “NB Max power” and “NB Optimum” techniques, although suboptimal for $B_w < 30$ GHz, provide almost constant rate for larger B_w . The best performance is provided by “Max-eig phase” which remains close to “UB” for all the considered bandwidths. The solution obtained through SDR performs similar to “NB Optimum” and significantly worse than “Max-eig phase”. Finally, we observe that the SCF algorithm does not provide excellent performance but this is not surprising. Indeed, although it is designed for solving the problem in (17), it is not guaranteed that its solution translates into an achievable rate higher than that provided by other techniques. In fact, the maximizer of (17) maximizes the upper bound to the rate, not the actual rate.

Remark 3: Please note that, for all considered techniques, the best performance is achieved when B_w is as small as possible. This corresponds to the case where the N_1 allocated sub-bands are adjacent (i.e., $B_w = N_1 \bar{B}$). However, we point out that due to system constraints, this situation might not occur in a scenario where many users compete for the same channel resources. In general, an evaluation of the trade-off between the benefit of having additional allocated sub-bands, and the drawback of larger B_w needs to be carefully addressed at system level.

For the same parameters as in Fig. 5, Fig. 6 shows the achievable rate when random power loading is employed across sub-bands, for $N_1 = 4$. In this case “Max-eig phase” shows performance similar to “NB optimum” and outperforms all the other techniques whereas “NB Central” provides slightly better performance than for $N_1 = 1$, although still being the worst technique for $B_w > 60$ GHz.

In Figure 7 we highlight the effect of multipath, i.e. the reflection by the wall, and shadowing (denoted as “ms” in the legend) on the rate performances, for the same system parameters as in Figure 5. As for the shadowing affecting the BS–IRS–UE and BS–wall–UE paths, we considered independent realizations of a lognormal distribution with variance $\sigma_{sh} = 2$. As expected, the contribution of the signal reflection by the wall is beneficial to the performance since it carries additional energy to the receiver. The rate increase is, however, limited to about 5%–10% when “Max-eig phase” technique is employed. Although “NB central” seems to be more benefitted by the signal reflection by the wall, with up to 70% rate increase in some cases, it shows, however, poor performance compared to “Max-eig phase”.

Figure 8 shows the rate R versus the IRS size L in the presence of multipath and shadowing, modeled as in Figure 7, for $M_1 = 16$, $B_w = 60$ GHz, $\phi_{BS} = 45^\circ$ and $\phi_{UE} = 30^\circ$. We observe that, for small IRS size, the “NB” techniques perform all very similarly and their performances are close to those achieved by “UB”, whereas they all tend to degrade for medium-to-large surfaces, i.e., $L > 1000$. Instead, the “Max-eig phase” technique performs better for large surfaces and shows some degradation for $L < 1000$. The same behavior can be observed in Figure 8(right), where $N_1 = 4$, although performance differences tend to reduce.

In Fig. 9 we assess the influence of the system geometry on performance by measuring the achievable rate as a

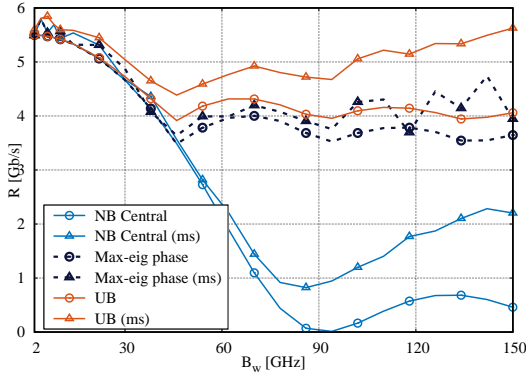


Fig. 7. Rate R versus B_w , for $K = 1$, $M_1 = 16$, $L = 64 \times 64$, $\phi_{BS} = 45^\circ$, $\phi_{UE} = 30^\circ$, $P_{1,s}^{tx} = 22$ dBm per sub-band, “equal power loading” and “Adapted beamforming” at the BS. The signal power spectral density is organized as in Figure 3(b) with $N_1 = 2$. The effect of shadowing and multipath (denoted as “ms” in the legend) is considered (triangle markers) or neglected (circle markers).

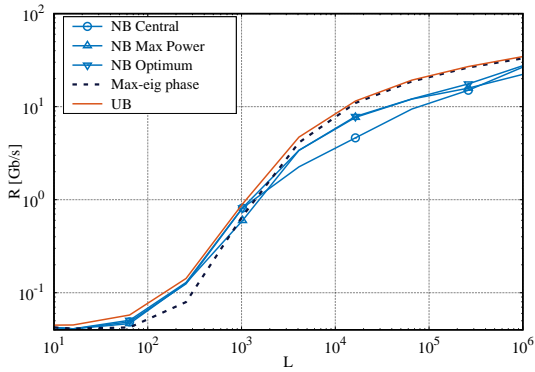


Fig. 8. Rate R versus the IRS size, L , in the presence of multipath and shadowing, for $K = 1$, $M_1 = 16$, $B_w = 60$ GHz, $\phi_{BS} = 45^\circ$, $\phi_{UE} = 30^\circ$, $P_{1,s}^{tx} = 22$ dBm per sub-band, “equal power loading” is adopted among the sub-bands and “Adapted beamforming” at the BS. The signal power spectral density is organized as in Figure 3(b) with $N_1 = 2$. The shadowing lognormal distribution has variance $\sigma_{sh} = 2$ dB.

function of the angle ϕ_{UE} (see Fig. 2), for $M_1=16$, $N_1=4$ allocated sub-bands, $P_{1,s}^{tx}=22$ dBm in each sub-band, “equal power loading” criterion on the sub-bands, shadowing with variance $\sigma_{sh} = 2$ dB and no wall reflection. The three figures refer to the cases $B_w=20$ GHz (left), $B_w=30$ GHz (center) and $B_w=60$ GHz (right). We first observe that, for $\phi_{UE} = 45^\circ$, all techniques behave the same, since the IRS acts as an ordinary mirror. Also, as ϕ_{UE} approaches 90° the rate tends to zero since the effective area of the IRS towards UE, varying with the cosine of ϕ_{UE} , tends to vanish. In general, in the range $45^\circ \leq \phi_{UE} \leq 90^\circ$ all techniques are almost equivalent, whereas for smaller angles there are significant difference among the performances they provide. The asymmetry of the curves w.r.t. $\phi_{UE} = 45^\circ$ is explained again by the dependency of the IRS effective area towards the UE by the cosine of ϕ_{UE} . Also in this case, the “Max-eig phase” technique always outperforms all the others, although “NB Optimum” provides the best trade-off between performance and implementation complexity.

E. Numerical results for a rank-2 matrix $\mathbf{G}(f)$

Fig. 10 show the results of simulation assuming a power spectral density as in (27), organized in sub-bands, with rank $K = 2$. This means that, for any $f \in \mathcal{B}$, the BS generates up to $K = 2$ beams. In order to support a rank-2 power spectral density matrix, the channel is required to have enough spatial diversity to grant a rank-2 matrix $\mathbf{Q}(f) = \mathbf{H}(f)\mathbf{G}(f)\mathbf{H}(f)^H$ as well. Then, the beamformers $\mathbf{v}_k(f)$ defined in (27) should generate sufficiently spatially separated beams for all $f \in \mathcal{B}$. For this reason, the results depicted in Fig. 10 refer to two IRSs of size 64×64 elements, both located on the wall and separated by 5 m from each other. These two IRSs, although physically separated, have to be considered as a single *logical* IRS of size $L = 128 \times 64$ elements. Hence, the analytic derivations presented in this work are still valid. In Fig. 10 we use $M_1 = 32$ transmit antennas, equal power loading among the sub-bands and $P_{k,s}^{tx} = 22$ dBm (about 160 mW) for each allocated sub-band and for each beam. That is, if the support of $g_k(f)$ is N_k sub-bands, $k = 1, 2$, the total transmit power is $160(N_1 + N_2)$ mW. We set $N_1 = N_2 = 2$ in Fig. 10(left), $N_1 = 4$ and $N_2 = 2$ in Fig. 10(center) and $N_1 = N_2 = 4$ in Fig. 10(right). In the figures the upper bound “UB” is computed using (12) whereas “Adapted beamforming” technique is applied at the BS using the beamforming vectors in (30), where the angles β_k , $k = 1, 2$, are the directions of the center of the two physical IRSs as observed from the center of the BS array. We first observe that for a rank-2 system the upper bound “UB” is less tight than in the rank-1 case. Indeed, especially in the cases $N_1 = N_2 = 2$ and $(N_1, N_2) = (4, 2)$, it shows a rate about 50% higher than that provided by the best technique, i.e., “Max-eig phase”. Also in this scenario, “Max-eig phase” outperforms all other techniques, especially when the number of allocated sub-bands is small. Specifically, for $N_1 = N_2 = 2$ “Max-eig phase” provides 20% rate increase w.r.t. “NB Optimum”, which is its best competitor. Such rate increase reduces to about 10% in the case $N_1 = 4$, $N_2 = 2$, whereas it is almost negligible for $N_1 = N_2 = 4$. Instead, the rate provided by “NB central” is almost linearly decreasing in all the considered cases.

F. Summary of the results

From the mathematical analysis introduced in Sections III and from the simulation results shown, we can summarize the following messages, which can be useful for the implementation of an IRS-aided UWB network:

- although beam squint at both BS and IRS play an important role, the system performance is also strongly affected by the system geometry, as can be observed by Figs. 4 and 9;
- the upper bound proposed in (12) is easy to compute and very tight, especially for single carrier ultra-wideband signals. For signals with power density profiles such as in Figure 3(b) the upper-bound is always very tight for relative bandwidths up to about 15% whereas the gap with “Max-eig phase” (the best performing technique) is noticeable for relative bandwidths greater than 15% (see Figs. 5 and 7). This gap, however, does not exceed 30%

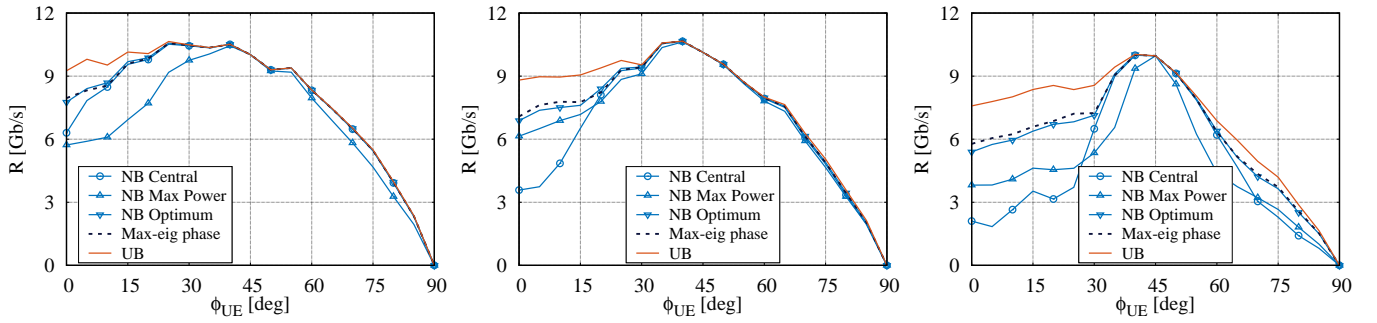


Fig. 9. Achievable rate, R , versus angle ϕ_{UE} for $\phi_{\text{BS}} = 45^\circ$ and $B_w \in \{18, 30, 60\}$ GHz from left to right. $N_1 = 4$ sub-bands are allocated to the single UE ($K = 1$) with “equal power loading” criterion and “Adapted beamforming” technique is adopted at the BS. Transmit power per sub-band is $P_{1,s}^{\text{tx}} = 22$ dBm. The shadowing lognormal distribution has variance $\sigma_{\text{sh}} = 2$ dB and there is no multipath.

of the rate in the worst case, and thus represents a good approximation of the system performance.

- the “NB central” technique is the simplest to implement and, for sparse-spectrum signals, provides performance near to the optimum for signal bandwidth $B_w < 30$ GHz. However, its performance dramatically drops for $B_w > 30$ GHz. Instead, for UWB single-carrier signals, it performs always close to the upper bound for all the considered range of relative bandwidths;
- the “NB Optimum” technique achieves, in general, good performance;
- the “SCF” algorithm, despite its complexity and its ability to provide a maximizer to (17), does not achieve superior performance in terms of rate, for it is most of the times worse or comparable to “Max-eig phase”;
- the SDR technique performs worse than “SCF”;
- the “Max-eig phase” solution seems to provide the best trade-off between performance and complexity for $B_w > 30$ GHz, large L , and a small number of allocated sub-bands, although, for very large L , its computational complexity might be unaffordable.

VI. CONCLUSIONS

We considered the problem of maximizing the achievable rate in a THz communication system where both BS and IRS may generate the beam-squint effect. We then proposed a set of techniques for configuring the IRS in the presence of wideband signals and compared against an upper bound. The channel model we used is realistic and specific for THz communication, accounting for multipath due to reflection from few large objects, molecular absorption, and shadowing. We specifically considered two important scenarios envisaged for 6G THz communications: i) the case of a single carrier UWB signal and ii) a multicarrier signal. We also provided an analytical condition granting the optimality of the “NB Central” solution, which is the simplest to implement. Our results pave the way for a fruitful application of IRSs and UWB signaling to wireless networks, and indicate that the spectrum allocation policy needs to take into account the system geometry and the IRS configuration in order to achieve information-theoretical performance.

APPENDIX A PROOF OF PROPOSITIONS 1 AND 2

The rate $R(\boldsymbol{\theta})$ in (6) can be rewritten as

$$\begin{aligned} R(\boldsymbol{\theta}) &= \int_{\mathcal{B}} \log \left| \mathbf{I} + \frac{1}{N_0} \mathbf{Q}(f, \boldsymbol{\theta}) \right| df \\ &= \int_{\mathcal{B}} \sum_{m=1}^{r_Q(f, \boldsymbol{\theta})} \log \left(1 + \frac{\lambda_{Q,m}(f, \boldsymbol{\theta})}{N_0} \right) df \end{aligned} \quad (31)$$

where the $M_2 \times M_2$ matrix $\mathbf{Q}(f, \boldsymbol{\theta}) = \mathbf{H}(f, \boldsymbol{\theta}) \mathbf{G}(f) \mathbf{H}^H(f, \boldsymbol{\theta})$ is positive definite, has rank $r_Q(f, \boldsymbol{\theta}) = \rho(\mathbf{Q}(f, \boldsymbol{\theta}))$ and has eigenvalues $\lambda_{Q,m}(f, \boldsymbol{\theta})$, $m = 1, \dots, r_Q(f, \boldsymbol{\theta})$. Given the system parameters and for every frequency f , once $\boldsymbol{\theta}$ is chosen, the eigenvalues $\lambda_{Q,m}(f, \boldsymbol{\theta})$ are known, as well as

$$P^{\text{rx}}(\boldsymbol{\theta}) = \int_{\mathcal{B}} \sum_{m=1}^{r_Q(f, \boldsymbol{\theta})} \lambda_{Q,m}(f, \boldsymbol{\theta}) df = \int_{\mathcal{B}} \text{Tr}\{\mathbf{Q}(f, \boldsymbol{\theta})\} df \quad (32)$$

which corresponds to the total received power. Then, we can bound $R(\boldsymbol{\theta})$ as follows:

$$R(\boldsymbol{\theta}) \leq \max_{\mathbf{y}(f)} \int_{\mathcal{B}} \sum_{m=1}^{r_Q(f)} \log \left(1 + \frac{y_m(f)}{N_0} \right) df \quad (33)$$

subject to $\int_{\mathcal{B}} \sum_{m=1}^{r_Q(f)} y_m(f) df = P^{\text{rx}}(\boldsymbol{\theta})$, $y_m(f) \geq 0$, $m = 1, \dots, r_Q(f)$, $\forall f \in \mathcal{B}$. Here $\mathbf{y}(f) = [y_1(f), \dots, y_{M_2}(f)]^T$ is a vector of auxiliary functions. Using (13), the maximization over $\mathbf{y}(f)$ in (33) can be solved by using the Euler-Lagrange formula. We obtain

$$R(\boldsymbol{\theta}) \leq \sum_{m=1}^{M_2} B_m \log \left(1 + \frac{P^{\text{rx}}(\boldsymbol{\theta})}{N_0 \sum_{m=1}^{M_2} B_m} \right) \quad (34)$$

and, by consequence, (10). As a special case, when the matrix $\mathbf{G}(f)$ is rank-1, it is clear that the matrix $\mathbf{Q}(f, \boldsymbol{\theta})$ is also rank-1. Hence $B_m = 0$ for $m = 2, \dots, M_2$, and (10) reduces to (15). As a final step, in order to evaluate the r.h.s. of (10) we need to solve the problem $\max_{\boldsymbol{\theta}} P^{\text{rx}}(\boldsymbol{\theta})$ i.e., we look for the IRS configuration, $\boldsymbol{\theta}$, maximizing the total received power. By

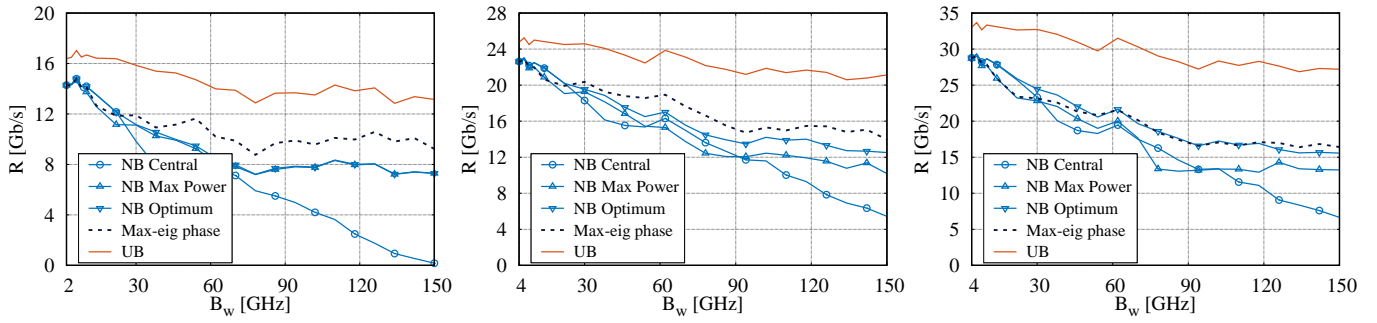


Fig. 10. Achievable rate, R , versus the available bandwidth B_w for a rank $K = 2$ matrix $\mathbf{G}(f)$, $M_1 = 32$, transmit power 22 dBm for each sub-band and each beam, with “equal power loading” among the sub-bands allocated to the user, and “Adapted beamforming” at the BS. $N_1 = N_2 = 2$ (left), $N_1 = 4$, $N_2 = 2$ (center) and $N_1 = 4$, $N_2 = 4$ (right).

recalling (8), the definition of $\mathbf{Q}(f, \boldsymbol{\theta})$, and (3) we can write

$$\begin{aligned} P^{\text{rx}}(\boldsymbol{\theta}) &= \int_{\mathcal{B}} \text{Tr} \{ \mathbf{H}(f, \boldsymbol{\theta}) \mathbf{G}(f) \mathbf{H}^{\text{H}}(f, \boldsymbol{\theta}) \} df \\ &= \boldsymbol{\gamma}^{\text{H}} \mathbf{T} \boldsymbol{\gamma} + w + 2\Re \{ \mathbf{q}^{\text{H}} \boldsymbol{\gamma} \} \end{aligned} \quad (35)$$

where $\boldsymbol{\gamma} = [\gamma_1, \dots, \gamma_L]^{\text{T}}$, $\gamma_\ell = e^{j\theta_\ell}$, $\ell = 1, \dots, L$, \mathbf{T} as in (9), and w and \mathbf{q} defined in (14), respectively. It follows that

$$\max_{\boldsymbol{\theta}} P^{\text{rx}}(\boldsymbol{\theta}) = \max_{\boldsymbol{\gamma}, |\gamma_\ell|=1, \forall \ell} (\boldsymbol{\gamma}^{\text{H}} \mathbf{T} \boldsymbol{\gamma} + w + 2\Re \{ \mathbf{q}^{\text{H}} \boldsymbol{\gamma} \}). \quad (36)$$

Since \mathbf{T} is positive definite and $\boldsymbol{\gamma}^{\text{H}} \mathbf{T} \boldsymbol{\gamma}$ is non-negative, an upper bound to (36) can be obtained by relaxing the L unimodular constraints $|\gamma_\ell| = 1$ to the single quadratic constraint $\boldsymbol{\gamma}^{\text{H}} \boldsymbol{\gamma} = L$. We get

$$\begin{aligned} &\max_{\boldsymbol{\gamma}, |\gamma_\ell|=1, \forall \ell} (\boldsymbol{\gamma}^{\text{H}} \mathbf{T} \boldsymbol{\gamma} + w + 2\Re \{ \mathbf{q}^{\text{H}} \boldsymbol{\gamma} \}) \\ &\leq \max_{\boldsymbol{\gamma}, \|\boldsymbol{\gamma}\|^2=L} \boldsymbol{\gamma}^{\text{H}} \mathbf{T} \boldsymbol{\gamma} + w + 2 \max_{\boldsymbol{\gamma}, |\gamma_\ell|=1, \forall \ell} \Re \{ \mathbf{q}^{\text{H}} \boldsymbol{\gamma} \} \quad (37) \\ &= L \lambda_T^{\text{max}} + w + 2 \sum_{q=1}^L |q_\ell| \quad (38) \end{aligned}$$

where λ_T^{max} is the largest eigenvalue of \mathbf{T} . A computable expression for $r_Q(f)$, the upper bound to $r_Q(f, \boldsymbol{\theta})$, for the model in (3)-(4) can be obtained as follows. The rank $r_Q(f, \boldsymbol{\theta})$ can be first upper-bounded by

$$\begin{aligned} r_Q(f, \boldsymbol{\theta}) &= \rho(\mathbf{H}(f, \boldsymbol{\theta}) \mathbf{G}(f) \mathbf{H}^{\text{H}}(f, \boldsymbol{\theta})) \\ &\leq \min \{ \rho(\mathbf{H}(f, \boldsymbol{\theta})), \rho(\mathbf{G}(f)) \}. \end{aligned} \quad (39)$$

Next, we recall (3) and (4) and observe that

$$\rho(\mathbf{H}(f, \boldsymbol{\theta})) \leq \min \left\{ M_2, \rho \left(\sum_{\ell=1}^L e^{j\theta_\ell} \mathbf{H}_\ell(f) \right) + \rho(\bar{\mathbf{H}}(f)) \right\}.$$

Since $\mathbf{H}_\ell(f)$ is a rank-1 matrix, $\forall \ell = 1, \dots, L$, we can write $\mathbf{H}_\ell(f) = \mathbf{v}_\ell(f) \mathbf{w}_\ell(f)^{\text{T}}$ for certain vectors $\mathbf{v}_\ell(f)$ and $\mathbf{w}_\ell(f)$ and, thus, $\sum_{\ell=1}^L e^{j\theta_\ell} \mathbf{H}_\ell(f) = \mathbf{V}(f) \boldsymbol{\Theta} \mathbf{W}(f)^{\text{T}}$ where $\mathbf{V}(f) = [\mathbf{v}_1(f), \dots, \mathbf{v}_L(f)]$, $\mathbf{W}(f) = [\mathbf{w}_1(f), \dots, \mathbf{w}_L(f)]$ and $\boldsymbol{\Theta}$ is a diagonal matrix whose entries are $e^{j\theta_\ell}$, $\ell = 1, \dots, L$. Since $\boldsymbol{\Theta}$ has rank L (it is diagonal with non-zero diagonal elements) we have $\rho(\mathbf{V}(f) \boldsymbol{\Theta} \mathbf{W}(f)^{\text{T}}) \leq \min \{ L, \rho(\mathbf{V}(f)), \rho(\mathbf{W}(f)) \}$. Then, we can upper-bound $r_Q(f, \boldsymbol{\theta})$ as (16).

APPENDIX B

PROOF OF PROPOSITION 3

The power spectral density matrix for a monochromatic signal at frequency f_0 can be written as $\mathbf{G}(f) = \mathbf{G}_0 \delta(f - f_0)$. By using (21), the entry (ℓ, ℓ') of matrix \mathbf{T} is given by

$$\begin{aligned} [\mathbf{T}]_{\ell, \ell'} &= \int_{\mathcal{B}} \text{Tr} \{ \mathbf{H}_\ell(f) \mathbf{G}(f) \mathbf{H}_{\ell'}^{\text{H}}(f) \} df \\ &= K_\ell K_{\ell'} \text{Tr} \{ \mathbf{A}(f_0) \mathbf{G}_0 \mathbf{A}^{\text{H}}(f_0) \} e^{j2\pi f_0(\tau_{\ell'} - \tau_\ell)}. \end{aligned}$$

Hence $\mathbf{T} = M_0 \mathbf{z} \mathbf{z}^{\text{H}}$ where $M_0 = \text{Tr} \{ \mathbf{A}(f_0) \mathbf{G}_0 \mathbf{A}^{\text{H}}(f_0) \}$, $\mathbf{z} = [z_1, \dots, z_L]^{\text{T}}$ and $z_\ell = K_\ell e^{-j2\pi f_0 \tau_\ell}$, $\ell = 1, \dots, L$. Since the coefficients K_ℓ are positive, the term $\boldsymbol{\gamma}^{\text{H}} \mathbf{T} \boldsymbol{\gamma}$ is given by

$$\boldsymbol{\gamma}^{\text{H}} \mathbf{T} \boldsymbol{\gamma} = M_0 \left| \sum_{\ell=1}^L z_\ell^* \gamma_\ell \right|^2 \leq M_0 \sum_{\ell=1}^L K_\ell^2, \quad (40)$$

where the equality is obtained for $\boldsymbol{\gamma} = \boldsymbol{\gamma}^{\text{NB}}(f_0)$ in (20). Therefore $\boldsymbol{\gamma}^{\text{NB}}(f_0)$ is the maximizer of $\boldsymbol{\gamma}^{\text{H}} \mathbf{T} \boldsymbol{\gamma}$ and, hence, the optimal solution for a monochromatic signal.

APPENDIX C

PROOF OF PROPOSITION 4

Let us compute entry (ℓ, ℓ') of matrix \mathbf{T} when (21) holds. We have:

$$\begin{aligned} [\mathbf{T}]_{\ell, \ell'} &= \int_{\mathcal{B}} \text{Tr} \{ \mathbf{H}_\ell(f) \mathbf{G}(f) \mathbf{H}_{\ell'}^{\text{H}}(f) \} df \\ &= K_\ell K_{\ell'} \int_{\mathcal{B}} \text{Tr} \{ \mathbf{C}(f) \} e^{j2\pi f(\tau_{\ell'} - \tau_\ell)} df \\ &= K_\ell K_{\ell'} e^{j2\pi f_0(\tau_{\ell'} - \tau_\ell)} \\ &\quad \cdot \int_{-\frac{B_w}{2}}^{\frac{B_w}{2}} \text{Tr} \{ \mathbf{C}(f + f_0) \} \cdot e^{j2\pi f(\tau_{\ell'} - \tau_\ell)} df. \end{aligned}$$

where $\mathbf{C}(f) \triangleq \mathbf{A}(f) \mathbf{G}(f) \mathbf{A}^{\text{H}}(f)$. Now, since the received signal spectrum is even around f_0 , the integral is real. Moreover, because of the assumption on the positive semi-definiteness of $\mathbf{G}(f)$, made in Section II, the trace in the integral is non-negative. Defining this trace as $M(f)$, we get

$$[\mathbf{T}]_{\ell, \ell'} = e^{j2\pi f_0(\tau_{\ell'} - \tau_\ell)} \int_{-\frac{B_w}{2}}^{\frac{B_w}{2}} K_\ell K_{\ell'} M(f) \cos(2\pi f(\tau_{\ell'} - \tau_\ell)) df. \quad (41)$$

If condition (22) is satisfied, the integrand is positive for every f , so that the integral is positive. Thus, we have

$$\mathbf{T} = \tilde{\mathbf{T}} \odot \gamma^{\text{NB}}(f_0) (\gamma^{\text{NB}}(f_0))^{\text{H}} \quad (42)$$

where $\tilde{\mathbf{T}}$ is a matrix with all entries real positive. The solution of (18) with such a matrix is well known to be $\gamma^{\text{NB}}(f_0)$ [25].

APPENDIX D PROOF OF PROPOSITION 5

We first observe that the solution of (18) does not change if we multiply the matrix \mathbf{T} by a constant, say $1/L$. So, when (25) is satisfied, we can write $\frac{1}{L}\mathbf{T} = \mathbf{Z}\mathbf{M}\mathbf{Z}^{\text{H}}$ where $\mathbf{M} = \text{diag}(M_1, \dots, M_S)$ and $\mathbf{Z} = [\mathbf{z}_1/\sqrt{L}, \dots, \mathbf{z}_S/\sqrt{L}]$. When $L \rightarrow \infty$, it is easy to see that $\frac{1}{L}\mathbf{z}_s^{\text{H}}\mathbf{z}_{s'} \rightarrow \delta_{s,s'}$, where $\delta_{s,s'}$ is the Kronecker δ function, unless $(f_s - f_{s'})\tau$ is semi-integer, a case which we exclude since it has vanishing probability as $L \rightarrow \infty$. Thus, for $L \rightarrow \infty$, $\mathbf{Z}\mathbf{M}\mathbf{Z}^{\text{H}}$ becomes the eigenvalue decomposition of \mathbf{T} and M_1, \dots, M_S its non-zero eigenvalues. Correspondingly, $\gamma^{\text{NB}}(f_{s^*})$ becomes the eigenvector associated with the largest eigenvalue, yielding

$$P^{\text{rx}}(\gamma^{\text{NB}}(f_{s^*})) = (\gamma^{\text{NB}}(f_{s^*}))^{\text{H}}\mathbf{T}\gamma^{\text{NB}}(f_{s^*}) \quad (43)$$

which is clearly the largest possible value for P^{rx} .

REFERENCES

- [1] A. Nordin, L. Dossi, A. Tarable, and G. Virone, "Near-field IRS configuration techniques for wideband signals and THz communications," in *2023 IEEE International Conference on Communications Workshops (ICC Workshops)*, 2023. doi: 10.1109/ICCWorkshops57953.2023.10283765 pp. 1198–1203.
- [2] K. M. S. Huq, S. A. Busari, J. Rodriguez, V. Frascolla, W. Bazzi, and D. C. Sicker, "Terahertz-enabled wireless system for beyond-5G ultrafast networks: A brief survey," *IEEE Network*, vol. 33, no. 4, pp. 89–95, 2019.
- [3] I. Ahmed, K. Shahid, and H. Khammari, "DRL based beam selection and hybrid beamforming for intelligent reflective surface assisted massive MIMO system," in *2023 IEEE 97th Vehicular Technology Conference (VTC2023-Spring)*, 2023, pp. 1–6.
- [4] M. Di Renzo *et al.*, "Smart radio environments empowered by reconfigurable AI meta-surfaces: an idea whose time has come," *EURASIP Journal Wireless Communication Networks*, vol. 129, May 2019.
- [5] T. Gong, P. Gavrilidis, R. Ji, C. Huang, G. C. Alexandropoulos, L. Wei, Z. Zhang, M. Debbah, H. V. Poor, and C. Yuen, "Holographic MIMO communications: Theoretical foundations, enabling technologies, and future directions," *IEEE Communications Surveys & Tutorials*, pp. 1–1, 2023.
- [6] B. Wang, F. Gao, S. Jin, H. Lin, G. Y. Li, S. Sun, and T. S. Rappaport, "Spatial-wideband effect in massive MIMO with application in mmwave systems," *IEEE Communications Magazine*, vol. 56, no. 12, pp. 134–141, 2018.
- [7] L. Dai, J. Tan, Z. Chen, and H. V. Poor, "Delay-phase precoding for wideband THz massive MIMO," *IEEE Transactions on Wireless Communications*, vol. 21, no. 9, pp. 7271–7286, 2022.
- [8] F. Gao, B. Wang, C. Xing, J. An, and G. Y. Li, "Wideband beamforming for hybrid massive MIMO terahertz communications," *IEEE Journal on Selected Areas in Communications*, vol. 39, no. 6, pp. 1725–1740, 2021.
- [9] R. Wang, Y. Yang, B. Makki, and A. Shamim, "A wideband reconfigurable intelligent surface for 5G millimeter-wave applications," 2023. doi: 10.48550/arXiv.2304.11572
- [10] S. Gong, X. Lu, D. T. Hoang, D. Niyato, L. Shu, D. I. Kim, and Y.-C. Liang, "Toward smart wireless communications via intelligent reflecting surfaces: A contemporary survey," *IEEE Communications Surveys & Tutorials*, vol. 22, no. 4, pp. 2283–2314, Apr. 2020.
- [11] W. Cai, R. Liu, Y. Liu, M. Li, and Q. Liu, "Practical modeling and beamforming for intelligent reflecting surface aided wideband systems," *IEEE Communications Letters*, vol. 24, no. 7, pp. 1568–1571, 2020.
- [12] S. Zeng, H. Zhang, B. Di, Y. Liu, M. D. Renzo, Z. Han, H. V. Poor, and L. Song, "Intelligent omni-surfaces: Reflection-refraction circuit model, full-dimensional beamforming, and system implementation," *IEEE Transactions on Comm.*, vol. 70, no. 11, pp. 7711–7727, 2022.
- [13] Y. Chen, D. Chen, and T. Jiang, "Beam-squint mitigating in reconfigurable intelligent surface aided wideband mmwave communications," in *2021 IEEE Wireless Communications and Networking Conference (WCNC)*, 2021, pp. 1–6.
- [14] D. Konstantinos, s. D. A. Styliano, Q. N. Hien, B. Boris, and M. Michail, "Intelligent reflecting surface-aided wideband THz communications: Modeling and analysis," *IEEE WCNC*, 2021. [Online]. Available: <https://arxiv.org/abs/2110.15768>
- [15] M. Cui, L. Dai, Z. Wang, S. Zhou, and N. Ge, "Near-field rainbow: Wideband beam training for XL-MIMO," *IEEE Transactions on Wireless Communications*, pp. 1–1, 2022.
- [16] W. Hao, F. Zhou, M. Zeng, O. A. Dobre, and N. Al-Dhahir, "Ultra wideband THz IRS communications: Applications, challenges, key techniques, and research opportunities," *IEEE Network*, vol. 36, no. 6, pp. 214–220, 2022.
- [17] S. Ma, W. Shen, J. An, and L. Hanzo, "Wideband channel estimation for IRS-aided systems in the face of beam squint," *IEEE Transactions on Wireless Communications*, vol. 20, no. 10, pp. 6240–6253, 2021.
- [18] H. Hashemi, T.-s. Chu, and J. Roderick, "Integrated true-time-delay-based ultra-wideband array processing," *IEEE Communications Magazine*, vol. 46, no. 9, pp. 162–172, 2008.
- [19] J. An, C. Xu, D. W. K. Ng, C. Yuen, L. Gan, and L. Hanzo, "Reconfigurable intelligent surface-enhanced OFDM communications via delay adjustable metasurface," *CoRR*, vol. abs/2110.09291, 2021. [Online]. Available: <https://arxiv.org/abs/2110.09291>
- [20] R. Fara, P. Ratajczak, D.-T. Phan-Huy, A. Ourir, M. Di Renzo, and J. de Rosny, "A prototype of reconfigurable intelligent surface with continuous control of the reflection phase," *IEEE Wireless Communications*, vol. 29, no. 1, pp. 70–77, 2022.
- [21] A. Tarable, F. Malandrino, L. Dossi, R. Nebuloni, G. Virone, and A. Nordin, "Optimization of IRS-aided sub-THz communications under practical design constraints," *IEEE Transactions on Wireless Communications*, vol. 21, no. 12, pp. 10824–10838, 2022.
- [22] J. Kokkonen, J. Lehtomäki, and M. Juntti, "Simple molecular absorption loss model for 200–450 gigahertz frequency band," in *2019 European Conference on Networks and Communications (EuCNC)*, 2019. doi: 10.1109/EuCNC.2019.8801950 pp. 219–223.
- [23] C. Han and Y. Chen, "Propagation modeling for wireless communications in the terahertz band," *IEEE Communications Magazine*, vol. 56, no. 6, pp. 96–101, 2018.
- [24] C. Pan, H. Ren, K. Wang, M. El-kashlan, A. Nallanathan, J. Wang, and L. Hanzo, "Intelligent reflecting surface aided mimo broadcasting for simultaneous wireless information and power transfer," *IEEE Journal on Selected Areas in Communications*, vol. 38, no. 8, pp. 1719–1734, 2020.
- [25] M. Soltanalian and P. Stoica, "Designing unimodular codes via quadratic optimization," *IEEE Transactions on Signal Processing*, vol. 62, no. 5, pp. 1221–1234, 2014.
- [26] O. Aldayel, V. Monga, and M. Rangaswamy, "Tractable transmit MIMO beamforming design under a constant modulus constraint," *IEEE Transactions on Signal Processing*, vol. 65, no. 10, pp. 2588–2599, 2017.
- [27] O. Özdoğan, E. Björnson, and E. G. Larsson, "Intelligent reflecting surfaces: Physics, propagation, and pathloss modeling," *IEEE Wireless Communications Letters*, vol. 9, no. 5, pp. 581–585, May 2020.
- [28] 3GPP, "5G; Study on channel model for frequencies from 0.5 to 100 GHz - Release 14," 3rd Generation Partnership Project (3GPP), Tech. Rep. 38.901, 2017.
- [29] ITU-R, "Attenuation by atmospheric gases and related effects," International Telecommunication Union, Recommendation p.676-13, 2022.
- [30] ITU-T, "Effects of building materials and structures on radiowave propagation above about 100 MHz," International Telecommunication Union, Recommendation P.2060-1, 2015.
- [31] A. Shafie, N. Yang, C. Han, J. M. Jornet, M. Juntti, and T. Kurner, "Terahertz communications for 6G and beyond wireless networks: Challenges, key advancements, and opportunities," *IEEE Network*, pp. 1–8, 2022.
- [32] Z.-q. Luo, W.-k. Ma, A. M.-c. So, Y. Ye, and S. Zhang, "Semidefinite relaxation of quadratic optimization problems," *IEEE Signal Processing Magazine*, vol. 27, no. 3, pp. 20–34, 2010.
- [33] Q. Wu and R. Zhang, "Intelligent reflecting surface enhanced wireless network: Joint active and passive beamforming design," in *2018 IEEE Global Communications Conference (GLOBECOM)*, 2018. doi: 10.1109/GLOCOM.2018.8647620 pp. 1–6.